Natural convection in vertical enclosures containing simultaneously fluid and porous layers

By C. BECKERMANN, R. VISKANTA AND S. RAMADHYANI

Heat Transfer Laboratory, School of Mechanical Engineering, Purdue University,
West Lafayette, IN 47907, USA

A numerical and experimental study is reported of natural convection in a vertical rectangular fluid enclosure that is partially filled with a fluid-saturated porous medium. Velocities, stresses, temperatures, and heat fluxes are assumed to be continuous across the fluid/porous-medium interface, and the conservation equations for the fluid and the porous regions are combined into a single set of equations for numerical solution. Thermocouples as well as a Mach–Zehnder interferometer are used to measure temperature distributions and infer fluid flow patterns within the fluid and the porous medium. For various test cells, porous-layer configurations and fluid–solid combinations, the model predictions show excellent agreement with the experimental measurements. It is found that the intensity of natural convection is always much stronger in the fluid regions, while the amount of fluid penetrating into the porous medium increases with increasing Darcy and Rayleigh numbers. The degree of penetration of fluid into the porous medium depends strongly on the porous-layer geometry and is less for a horizontal porous layer occupying the lower half of the test cell. If penetration takes place, the flow patterns in the fluid regions are significantly altered and the streamlines show cusps at the fluid/porous-medium interfaces. For a high effective-thermal-conductivity porous medium, natural convection in the medium is suppressed, while the isotherms bend sharply at the fluid/porous-medium interface.

1. Introduction

Natural-convection heat transfer and fluid flow in a system containing simultaneously a fluid reservoir and a porous medium saturated with the same fluid is of great mathematical and practical interest. Applications include solidification of castings, crude-oil production, ground-water pollution, thermal insulation, geophysical systems, etc. For example, if a porous insulation occupies only a small fraction of the space between two walls, the fluid flow and heat transfer can be significantly reduced because of the large frictional resistance offered by the porous insulation. Penetration of fluid into a porous medium is also important in a solidifying alloy casting. Because of the extended freezing temperature range of an alloy, a mushy zone might exist, consisting of a fine meshwork of dendrites growing into the melt. Fluid flow between this porous mushy zone and the pure melt region will eventually alter the chemical homogeneity and grain structure of the solidified casting. In addition, the problem is of fundamental interest from an experimental point of view. By observing the convection in the fluid region information can be deduced about the heat transfer and fluid flow in the porous region and between the two regions. The present study is concerned with natural convection in a two-
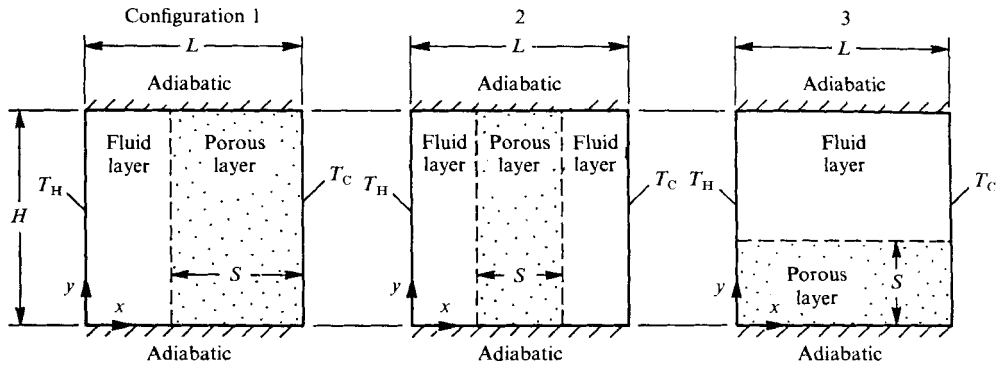
FIGURE 1. Schematic of the physical model and coordinate system.

dimensional, rectangular fluid enclosure with the vertical walls held at different temperatures and the connecting horizontal walls considered adiabatic. The enclosure is partially filled with various vertical or horizontal layers of a porous material as shown in figure 1.

Mathematically, the problem involves the coupling of the momentum equation for the fluid region (i.e. the Navier–Stokes equation) with the equation for the porous medium (typically some form of Darcy's law) through an appropriate set of matching conditions at the fluid/porous-layer interface. Depending on the chosen form of the momentum equation for the porous medium, the two sets of differential equations may be of different order, necessitating the use of empirical matching conditions. In the case where the flow in the porous medium is assumed to be governed by Darcy's law, Beavers & Joseph (1967) proposed the use of a 'slip-flow' matching condition with the slip velocity proportional to the shear rate at the interface. For a two-dimensional, orthogonal coordinate system (n, t), where n and t are the coordinates normal and tangential to the fluid/porous-medium interface, respectively, these matching conditions can be written as

$$U^n = U_D^n,$$
(1a)

$$\frac{\partial U^t}{\partial n} + \frac{\partial U^n}{\partial t} = \frac{\gamma}{K^{\frac{1}{2}}}(U^t - U_D^t),$$
(1b)

$$-P + 2\mu \frac{\partial U^n}{\partial n} = -P_D,$$
(1c)

where $U = (U^n, U^t)$ is the velocity vector in the fluid region, while $U_D = (U_D^n, U_D^t)$ is the Darcian velocity vector in the porous medium (i.e. volume flow rate per unit cross-sectional area). In the above equations, K is the permeability, μ is the dynamic viscosity of the fluid, and γ is an empirical parameter characterizing the porous medium; P and P_D represent the local thermodynamic pressures in the fluid and the porous medium, respectively. Derjani, Taslim & Narusawa (1986) and Nield (1977, 1983) have used Darcy's law together with the above matching conditions to study convective and thermal instabilities of superposed porous and fluid layers heated from below. Masuoka (1974) has observed convective currents in a layer of fluid heated from below and divided by a horizontal porous wall. He has found that the

porous wall suppresses the onset of thermal instabilities, which has also been confirmed by an approximate analysis based on Darcy's law.

Neale & Nader (1974) argued that, at the interface, the tangential components of the velocity in the fluid (U^t) and of the Darcian velocity in the porous medium (U_D^t) are actually equal and there exists no slip-flow. Owing to this no-slip condition, velocity gradients may be induced in the porous medium adjacent to the interface, making Darcy's law inapplicable. Hence, they proposed the use of the Brinkman-extended Darcy equations (Brinkman 1949) to account for the macroscopic viscous stress in the porous medium (as opposed to the viscous effects induced by the solid matrix and modelled by Darcy's term). Furthermore, they suggested that, at the interface, the macroscopic viscous shear stress in the porous medium (modelled through Brinkman's extension) is equal to the shear stress on the fluid side. Extending the arguments of Neale & Nader (1974) to two-dimensional flow, the matching conditions at the fluid/porous-layer interface can be expressed in general form as

$$U^n = U_D^n, \quad U^t = U_D^t, \tag{2a}$$

$$\mu\left(\frac{\partial U^t}{\partial n} + \frac{\partial U^n}{\partial t}\right) = \mu_{\text{eff}}\left(\frac{\partial U_D^t}{\partial n} + \frac{\partial U_D^n}{\partial t}\right), \tag{2b}$$

$$-P + 2\mu\frac{\partial U^n}{\partial n} = -P_D + 2\mu_{\text{eff}}\frac{\partial U_D^n}{\partial n}, \tag{2c}$$

where the effective viscosity of the fluid saturated porous medium, μ_{eff}, is, in general, not equal to the fluid viscosity μ. For Poiseuille flow in a channel with a permeable wall it has been recognized (Neale & Nader 1974) that the two approaches, the 'slip-flow' and the no-slip matching conditions, yield identical end results for $\gamma = (\mu_{\text{eff}}/\mu)^{\frac{1}{2}}$. There have been many attempts to derive expressions for the viscosity ratio as a function of the properties of the porous medium (Lundgren 1972; Koplik, Levine & Zee 1983; Kim & Russel 1985). Most analyses predict the effective viscosity to be greater than the fluid viscosity (Kim & Russel 1985), but it has been found that taking $\mu_{\text{eff}} = \mu$ provides good agreement with experimental data (Neale & Nader 1974).

Somerton & Catton (1982) and Catton (1985) have used the Brinkman-extended Darcy equations together with the Neale & Nader (1974) matching conditions to investigate the stability and heat transfer in superposed horizontal porous and fluid layers with internal heat generation in the porous medium and heating from below. They have predicted that the fluid layer above the porous bed is destabilizing and can induce motion in the porous bed. Nishimura *et al.* (1986) have studied natural convection in a vertical enclosure heated and cooled from the sides and horizontally divided into fluid and porous regions. The Navier-Stokes equation for the fluid layer and the Brinkman-extended Darcy equation for the porous layer have been matched explicitly by assuming continuity of velocity, shear stress and pressure at the interface. Their numerical results, obtained utilizing a finite-element method, have been found to be in good agreement with experiments conducted using silicone oil and glass beads. Their experiments have been limited, however, to conditions in which the heat transfer in the porous region is dominated by conduction.

Beckermann, Ramadhyani & Viskanta (1986a) have performed a numerical and experimental study of natural convection between vertical fluid and porous layers inside a vertical rectangular enclosure. By assuming the validity of the Neale & Nader (1974) matching conditions, they have combined the governing equations for

the fluid and porous layers into one set of equations valid for the entire domain. Since their numerical algorithm ensures continuity of the velocities and stresses at every point in the computational domain, the matching conditions, expressed in (2), are satisfied automatically. The numerical results have shown good agreement with flow visualization and temperature measurements. They have concluded that for a vertical porous layer occupying half of the test cell, the degree of penetration of fluid into the porous layer depends, roughly, on the product of the Rayleigh and Darcy numbers, which should be greater than about 50 for penetration to be significant. Arquis & Caltagirone (1984) and Arquis, Caltagirone & Langlais (1986) have used an approach similar to that of Beckermann *et al.* (1986*a*) to study natural convection in a cavity containing various vertical fluid and porous layers. By considering the porous medium as a 'special' fluid, only one set of conservation equations has been solved for the entire domain. The transition from the fluid to the porous region has been achieved by a continuous variation in space of the permeability and other 'structural' parameters. The few experiments performed by Arquis *et al.* (1986) reveal good agreement between measured and numerically predicted overall heat transfer rates across the cavity.

There have been numerous studies of natural convection in vertical and horizontal enclosures containing various layers of porous media having different permeabilities (Poulikakos & Bejan 1983; McKibbin & O'Sullivan 1981; Rana, Horne & Cheng 1979; Reda 1985; Gjerde & Tyvand 1984; Somerton & Goff 1985). These studies are of related interest because a layer of high permeability is expected to have a similar effect on the fluid flow in the enclosure as a pure fluid layer. In fact, most investigations show that the flow takes place primarily in the layers of higher permeability, i.e. the flow is channelled. In addition, the discontinuities in the permeability (and the effective thermal conductivity) between adjacent porous layers cause cusps in both streamline and isotherm patterns.

The foregoing discussion illustrates that little is known about natural-convection fluid flow and heat transfer in enclosures containing simultaneously fluid and porous layers. Through combined experimental and analytical work, the present study is aimed at investigating the global physical phenomena occurring in such systems. In order to study the effect of the configuration of the fluid and porous layers on the natural-convection patterns, various horizontal and vertical layers of a porous medium are constructed within a fluid-filled vertical enclosure (see figure 1). The influence of the material properties is investigated by employing different combinations of porous media (glass and aluminium beads) and fluids (water and glycerin). In the experiments, a Mach–Zehnder interferometer is used to obtain a complete record of the temperature field in the fluid regions. It is also utilized as a flow-visualization device to determine the flow patterns in the fluid regions as well as the extent of penetration of fluid into the porous layer. Numerical simulations are performed to supplement the experimental results. The flow and heat transfer are modelled by combining the governing equations for the porous and fluid regions into a single set of equations valid for the entire domain. This is accomplished by assuming the validity of the Neale & Nader (1974) interface conditions (see (2)) for the velocities and stresses as well as by matching the temperatures and heat fluxes at the interface. The combined equations contain a binary 'existence' parameter through which the transition from one region into another is achieved. The numerical results are verified by comparing them to temperature measurements taken in both the fluid and the porous layer. The ability of the present model to simulate natural convection in enclosures partially filled with a porous medium is discussed. However,

in view of the large number of governing parameters, no attempt is made to present a complete parametric study.

2. Analysis
2.1. *Model equations*

The three physical situations considered in the present study are shown in figure 1. In all cases, the vertical walls of the enclosure are of height H and are held at the temperatures $T_{\rm H}$ and $T_{\rm C}$. The connecting horizontal walls of length L are considered adiabatic. The porous layers within the two-dimensional cavity are of thicknesses S. In case 1, the porous layer extends from the (right) cold wall, while in case 2 the layer is centred on the vertical midplane of the enclosure and is bounded by two vertical fluid layers. The porous layer in case 3 is horizontal and covers the entire bottom wall of the cavity.

In the analysis, the porous medium is considered to be homogeneous and isotropic. The fluid within the porous medium saturates the solid matrix and both are in local thermodynamic equilibrium. The flow is assumed to be steady, laminar, incompressible, and two-dimensional. The thermophysical properties of the fluid and the effective properties of the porous medium are assumed constant, except for the density in the buoyancy term in the momentum equations. With the foregoing assumptions, the governing equations for the fluid are

$$\mathbf{\nabla}\cdot\mathbf{U} = 0, \tag{3}$$

$$\rho(\mathbf{U}\cdot\mathbf{\nabla})\,\mathbf{U} = -\mathbf{\nabla}P + \mathbf{\nabla}\cdot(\mu\mathbf{\nabla}\mathbf{U}) + \rho\mathbf{g}\beta(T - T_{\rm C}), \tag{4}$$

$$\rho c_p(\mathbf{U}\cdot\mathbf{\nabla}T) = \mathbf{\nabla}\cdot k\mathbf{\nabla}T), \tag{5}$$

where ρ, c_p, k and β are the density, specific heat, thermal conductivity and isobaric coefficient of thermal expansion of the fluid. In the above equations, $\mathbf{U} = (U, V)$, T and P are the velocity, temperature and pressure in the fluid, respectively.

The conservation equations for the porous layer are based on a non-Darcian model, incorporating the Brinkman and Forchheimer extensions. The importance of these extensions is discussed in Beckermann, Viskanta & Ramadhyani (1986*b*). Their computations show that for the conditions of some of the present experiments (see table 1), Brinkman's extension is small compared to the Darcy term. However, Brinkman's extension has been included in all the computations to ensure continuity of the velocities and stresses at the fluid/porous-medium interface. Forchheimer's extension (Forchheimer 1901) serves to model the inertia and, hence, Prandtl-number effects on the flow in the porous medium. Although the effect of Forchheimer's extension is significant mainly at low Prandtl numbers, it has been utilized in all the computations of the present study. It should be be noted that both extensions must be included simultaneously for a high-permeability porous medium (i.e. a high Darcy number) (Beckermann *et al.* 1986*b*). In terms of the (superficial) Darcian velocity, $\mathbf{U}_{\rm D} = (U_{\rm D}, V_{\rm D})$, the governing equations for the porous medium can be written as

$$\mathbf{\nabla}\cdot\mathbf{U}_{\rm D} = 0, \tag{6}$$

$$0 = -\mathbf{\nabla}P_{\rm D} + \mathbf{\nabla}\cdot(\mu_{\rm eff}\,\mathbf{\nabla}\mathbf{U}_{\rm D}) + \rho\mathbf{g}\beta(T - T_{\rm C}) - \left(\frac{\mu}{K} + \frac{\rho C}{K^{\frac{1}{2}}}|\mathbf{U}_{\rm D}|\right)\mathbf{U}_{\rm D}, \tag{7}$$

$$\rho c_p(\mathbf{U}_{\rm D}\cdot\mathbf{\nabla}T) = \mathbf{\nabla}\cdot(k_{\rm eff}\,\mathbf{\nabla}T), \tag{8}$$

where $\mu_{\rm eff}$ and $k_{\rm eff}$ are the effective viscosity and thermal conductivity of the porous medium, respectively, while C and K are the inertia coefficient and the permeability.

The value of the permeability K can be determined from the Kozeny–Carman equation for packed beds of beads of diameter d_b and porosity (i.e. liquid fraction) ϵ,

$$K = \frac{d_b^2 \epsilon^3}{175(1-\epsilon)^2}. \tag{9}$$

According to Ergun (1952), the inertia coefficient C can be calculated from the following empirical formula:

$$\frac{C}{K^{\frac{1}{2}}} = \frac{1.75(1-\epsilon)}{\epsilon^3 d_b}. \tag{10}$$

In addition, models for the effective properties (μ_{eff} and k_{eff}) of the porous medium are needed. As a first approximation and owing to lack of conclusive information, μ_{eff} is taken equal to the fluid viscosity μ in the present study. For a large variety of porous matrices (including glass and aluminium beads) and fluids, D. Lindemann (1986, private communication) has found best agreement between measured and calculated values of the (stagnant) effective thermal conductivity using the empirical relationship (Combarnous & Bories 1975)

$$k_{\text{eff}} = \mathrm{k}^{\epsilon} k_b^{(1-\epsilon)}, \tag{11}$$

where k_b is the thermal conductivity of the solid matrix (i.e. beads). Equation (11) is utilized in all calculations of the present study. Because of the relatively small velocities encountered in the present experiments, thermal dispersion effects can safely be neglected.

2.2. Combined equations

The conservation equations for the fluid and the porous regions must be coupled by an appropriate set of matching conditions at the fluid/porous-medium interface. According to the discussion presented in §1, the matching conditions for the momentum equations are given by (2). The energy equations are coupled by the conditions of continuity of temperature and heat flux (Beckermann *et al.* 1986*a*). Because the velocities, stresses, temperatures and heat fluxes are continuous across the fluid/porous-medium interface, the fluid and the porous regions can be treated as a single (continuous) domain governed by one set of conservation equations. In writing one set of equations valid for the entire domain, the different forms of the conservation equations for the fluid and the porous regions (refer to the previous section) must, however, be accommodated. This can easily be accomplished by introducing the following binary parameter:

$$X_p(\xi, \eta) = \begin{cases} 1 & \text{if in porous medium,} \\ 0 & \text{if in fluid.} \end{cases} \tag{12}$$

The governing equations for the fluid and the porous medium can now be combined into one set of conservation equations. In dimensionless form, we have

$$\nabla \cdot \boldsymbol{u} = 0, \tag{13}$$

$$(1-X_p)\left[(\boldsymbol{u} \cdot \nabla)\boldsymbol{u}\right] = -\nabla p + Pr\nabla^2 \boldsymbol{u} + Ra\,Pr\Theta\boldsymbol{e}_\eta - X_p\left(\frac{Pr}{Da} + \frac{C}{Da^{\frac{1}{2}}}|\boldsymbol{u}|\right)\boldsymbol{u}, \tag{14}$$

$$\boldsymbol{u} \cdot \nabla\Theta = (X_p(R_k-1)+1)\,\nabla^2\Theta, \tag{15}$$

where $\boldsymbol{u}$ represents the Darcian velocity on the porous medium side and the true fluid

velocity on the fluid side. In the above equations, the dimensionless variables are defined as

$$\xi = \frac{x}{L}, \quad \eta = \frac{y}{L}, \quad u = \frac{UL}{\alpha} \text{ or } \frac{U_{\mathrm{D}} L}{\alpha}, \left.\begin{array}{c} \\ \\ \end{array}\right\}$$

$$\Theta = \frac{T - T_{\mathrm{C}}}{T_{\mathrm{H}} - T_{\mathrm{C}}}, \quad p = \frac{PL^2}{\rho\alpha^2} \text{ or } \frac{P_{\mathrm{D}} L^2}{\rho\alpha^2}, \left.\begin{array}{c} \\ \\ \end{array}\right\} \tag{16}$$

where $\alpha = k/(\rho c_p)$. Note that the governing equations are non-dimensionalized using the same scales for the variables in the fluid and porous regions. This procedure might result in physically unrealistic scales for one of the regions, but it greatly simplifies the writing of the combined equations. The dimensionless parameters in (13)–(15) are defined as

$$Ra = \frac{\rho g \beta (T_{\mathrm{H}} - T_{\mathrm{C}}) L^3}{\mu \alpha} \qquad \text{Rayleigh number,}$$

$$Da = \frac{K}{L^2} \qquad \text{Darcy number,}$$

$$Pr = \frac{c_p \mu}{k} \qquad \text{Prandtl number,}$$

$$R_k = \frac{k_{\mathrm{eff}}}{k} \qquad \text{thermal-conductivity ratio.}$$

By combining the conservation equations as suggested, the matching conditions at the fluid/porous-medium interface are satisfied automatically. The boundary conditions for the combined equations are given in dimensionless form as

$$\begin{array}{llll} \Theta = 1, & u = 0 & \text{at } \xi = 0, & 0 \leqslant \eta \leqslant A, \\ \Theta = 0, & u = 0 & \text{at } \xi = 1, & 0 \leqslant \eta \leqslant A, \\ \dfrac{\partial \Theta}{\partial \eta} = 0, & u = 0, & \text{at } \eta = 0 \text{ and } A, & 0 \leqslant \xi \leqslant 1, \end{array}\left.\right\} \tag{17}$$

where $A = H/L$ is the aspect ratio.

2.3. *Numerical procedure*

The combined conservation equations (13)–(15) were solved numerically utilizing the iterative SIMPLER algorithm (Patankar 1980). This algorithm is based on a control-volume formulation which ensures continuity of the mass, momentum and heat fluxes across the control surfaces and, thus, the fluid/porous-medium interface. The harmonic mean formulation adopted for the interface diffusion coefficients between two control volumes yields physically realistic results for abrupt changes in these coefficients (for example, if $R_k \neq 1$) without requiring an excessively fine grid in the neighbourhood of the fluid/porous-medium interface.

The mesh size required for sufficient numerical accuracy depended mainly on the Rayleigh (Ra) and Darcy (Da) numbers. A grid of 26×26 nodal points was utilized in the simulations of the experiments (refer to §4). Calculations performed on a 50×50 grid (Beckermann *et al.* 1986a) did not significantly improve the accuracy of the numerical results. The nodal points were uniformly distributed in the

η – direction, while the distribution along the ξ – direction was slightly skewed to have a greater concentration of points near the hot and cold vertical boundaries. The iterations were terminated when the dependent variables agreed to four significant digits at each nodal point. Convergence of the numerical solutions was also checked by performing overall mass and energy balances. The calculations were performed on a CYBER 205 computer and required less than 500 CPU seconds. Extensive tests of the accuracy of the numerical algorithm were performed for the limiting cases of fully fluid and fully porous enclosures (Beckermann *et al.* 1986*a*) and good agreement with results reported in the literature was found.

3. Experimental conditions and measurements

Experiments were performed in two different test cells of square cross-section. The smaller test cell, which was used for the interferometric studies, had inside dimensions of 4.76 cm in height and width and 3.81 cm in depth. The horizontal top and bottom walls were constructed of phenolic plates, while the vertical front and back walls were made of 6.35 mm thick high-quality optical glass. The larger test cell was utilized for the temperature measurements and had inside dimensions of 11.43 cm in height and width and 3.97 cm in depth. The horizontal top and bottom walls and the vertical front and back walls were made of acrylic plates which were held in place by a stainless-steel frame. In both test cells, the two vertical sidewalls, which served as the heat source/sink, were multipass heat exchangers machined out of a copper plate. By circulating a mixture of alcohol and water from two constant-temperature baths (Haake A82) through the two heat exchangers, the vertical sidewalls could be maintained at different temperatures. The temperatures of each copper heat exchanger were measured with three thermocouples epoxied separately into small-diameter holes which were drilled close to the surface of the copper plate facing the fluid. In all experiments, the temperatures of the heat exchangers were uniform to within 3% of the total temperature difference across the test cell. Both test cells were insulated with 5.09 cm thick Styrofoam. The insulation covering the front and back walls of the smaller test cell could be removed while performing the interferometric measurements.

The temperature distribution in the larger test cell was measured using a movable thermocouple probe sheathed in a 1.27 mm OD stainless-steel tube. The probe was mounted on an x–y translation stage allowing the position of the thermocouple bead in the test cell to be determined to within 0.5 mm. Temperatures were measured along the vertical centreplane of the test cell. After each movement of the thermocouple probe, the system was allowed to reach steady state again. Although the structure of the porous medium was slightly disturbed owing to the displacement of a bead by the probe, it is felt that the resulting error in the temperature measurements within the porous medium was relatively small considering the small diameter of the probe compared to the size of the porous layers (and the test cell). All thermocouples were calibrated with an accuracy of ± 0.1 °C.

Qualitative temperature distributions and flow-visualization measurements in the smaller test cell were obtained using a Mach–Zehnder interferometer with 10 cm diameter optics. The light source consisted of a collimated beam from a helium–neon laser ($\lambda = 632.8$ mm). The beam was split into two components, one of which passed through the test cell and was subsequently recombined with the second component, which moved along a reference path. The interference fringe pattern resulting from the recombined beams was imaged on a white glass plate and photographed using a

Experiment	Configuration	$s = S/L$	Test cell	Fluid	Beads ϕ (mm)	Ra	Da	Pr	R_κ	C
1	1	0.5	Large	Glycerin	6.0 glass	9.52×10^5	2.248×10^{-6}	8356.2	2.259	0.565
2	1	0.5	Large	Glycerin	6.35 Al	9.52×10^5	2.518×10^{-6}	8356.2	17.10	0.565
3	2	0.33	Large	Glycerin	6.0 glass	9.52×10^5	2.248×10^{-6}	8356.2	2.259	0.565
4	2	0.33	Large	Glycerin	6.35 Al	9.52×10^5	2.518×10^{-6}	8356.2	17.10	0.565
5	3	0.5	Large	Glycerin	6.0 glass	9.52×10^5	2.248×10^{-6}	8356.2	2.259	0.565
6	3	0.5	Large	Glycerin	6.35 Al	9.52×10^5	2.518×10^{-6}	8356.2	17.10	0.565
7	1	0.5	Small	Water	1.5 glass	3.70×10^6	7.242×10^{-7}	6.44	1.372	0.588
8	1	0.5	Small	Water	6.0 glass	3.70×10^6	1.370×10^{-5}	6.44	1.362	0.554
9	1	0.5	Small	Water	3.16 Al	3.70×10^6	3.324×10^{-6}	6.44	40.21	0.581
10	1	0.5	Small	Water	6.35 Al	3.70×10^6	1.534×10^{-5}	6.44	37.47	0.554
11	2	0.33	Small	Water	1.5 glass	3.70×10^6	7.242×10^{-7}	6.44	1.372	0.588
12	2	0.33	Small	Water	6.0 glass	3.70×10^6	1.370×10^{-5}	6.44	1.362	0.554
13	2	0.33	Small	Water	3.16 Al	3.70×10^6	3.324×10^{-6}	6.44	40.21	0.581
14	2	0.33	Small	Water	6.35 Al	3.70×10^6	1.534×10^{-5}	6.44	37.47	0.554
15	3	0.5	Small	Water	1.5 glass	3.70×10^6	7.242×10^{-7}	6.44	1.372	0.588
16	3	0.5	Small	Water	6.0 glass	3.70×10^6	1.370×10^{-5}	6.44	1.362	0.554
17	3	0.5	Small	Water	3.16 Al	3.70×10^6	3.324×10^{-6}	6.44	40.21	0.581
18	3	0.5	Small	Water	6.35 Al	3.70×10^6	1.534×10^{-5}	6.44	37.47	0.554

TABLE 1. Summary of experimental test conditions

high-sensitivity film (Kodak Tri X-Pan). Owing to the blocking of the test beam by the porous medium, it was not possible to perform interferometric measurements within the porous medium. When viewing the interferograms, several extraneous features should be ignored. Owing to the relatively large test-cell depth, the fringe density in certain regions of the interference pattern is very high, making a quantitative interpretation of the interferograms difficult. In addition, the test beam might be slightly refracted due to the gradients of the refractive index in the fluid. This problem is especially serious in the thermal boundary layers along the vertical hot and cold sidewalls resulting in a distortion of the images of the test-cell boundaries. The problems, however, do not restrict the qualitative interpretation of the interferograms presented in §4.

The porous media consisted of random packings of spherical glass or aluminium beads ranging from 1.6 mm to 6.35 mm in diameter (refer to table 1). The thermophysical properties corresponding to the chemical composition of the beads are known (Weaver 1985). In configurations 1 and 2 (refer to figure 1) the vertical layers of beads were held in place by fine fibreglass (in case of the glass beads) or aluminium (in case of the aluminium beads) screens which were supported by small-diameter glass or aluminium rods. The porosity of the screen was much higher than the porosity of the beads, while the mesh size was only slightly smaller than the diameter of the beads. It is believed that the screens had a negligible influence on the flow and heat transfer between the fluid and the porous medium. In configuration 3, the beads were simply dropped into the test cell to form a horizontal layer of the desired height. The porosity (i.e. liquid fraction) of the porous layers was measured separately for each combination of beads and test cells. For the large-diameter beads and the small test cell, the increase in porosity near the walls was more significant, resulting in a higher value of the average porosity.

The fluids used were once-distilled, degasified water for the smaller test cell (for the interferometric studies) and chemical-grade glycerin for the larger test cell. With the various combinations of fluids, beads, porous-layer configurations, and test cells, it was possible to cover a relatively broad range of the relevant dimensionless parameters. The experimental conditions together with the values of the dimensionless parameters are summarized in table 1. All fluid properties were evaluated at a temperature of $\frac{1}{2}(T_{\mathrm{H}} + T_{\mathrm{C}})$.

Before each experiment, the screens were inserted into the test cell at the desired position and the resulting layer was filled with the beads. Then, the fluid was carefully siphoned into the test cell to ensure that no air was trapped in the matrix and to prevent air from mixing with the fluid. After switching on the constant-temperature baths, the system was allowed to reach steady state for at least 12 hours. The temperatures of the heat exchangers were monitored continuously to ensure that the desired temperature levels were maintained.

4. Results and discussion

4.1. *Comparison of measured and predicted temperatures*

In order to compare quantitatively measured and predicted temperatures, six experiments were performed in the larger test cell using glycerin as the fluid. For each configuration, two different porous media were employed: 6.0 mm diameter glass beads and 6.35 mm diameter aluminium beads (refer to table 1, experiments, 1–6). In these experiments, the temperature difference between the vertical hot and cold walls was kept at 10 °C. As may be seen from table 1, the Rayleigh, Darcy, and
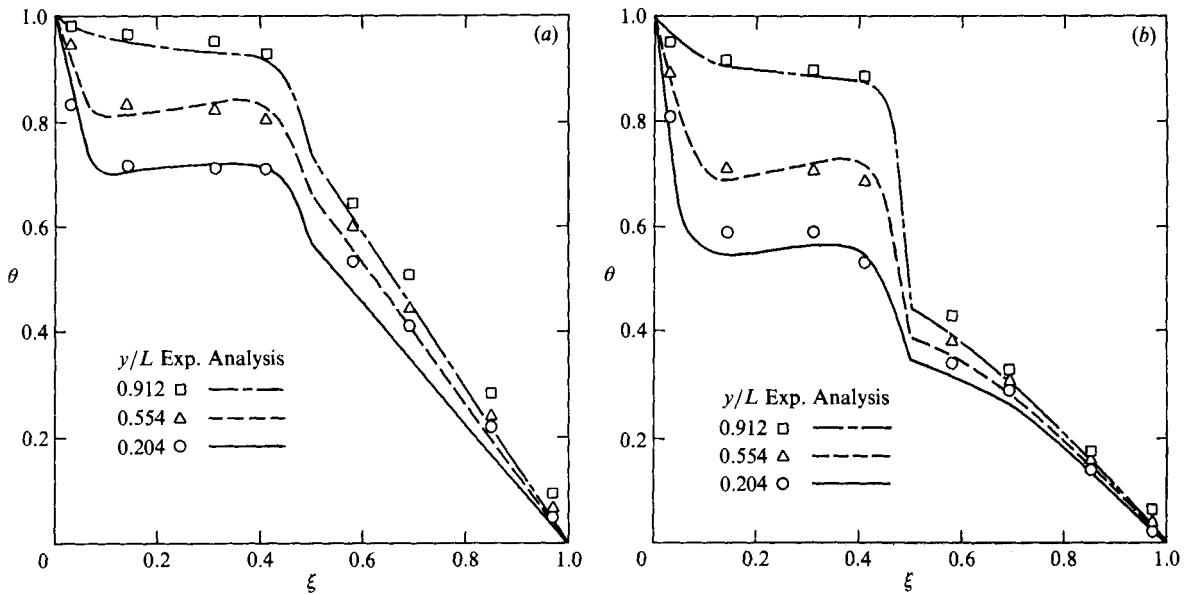
FIGURE 2. Experimental and predicted temperature profiles for configuration 1: (a) Experiment 1; (b) Experiment 2.

Prandtl numbers were approximately constant for experiments 1–6, while the thermal conductivity ratio R_k for the aluminium beads was much greater than for the glass beads. Temperature measurements were taken at three different heights from the bottom of the larger test cell. The results of these experiments, together with the pertinent numerical predictions are shown in figures 2–4.

From both the measured and predicted temperatures, it can be seen that, for all three configurations of the porous layer and both glass and aluminium beads, the temperature profiles inside the porous layers are basically straight lines, indicating that heat transfer is mainly by conduction and very little fluid penetrates into the porous layers. In the case of the glass beads, the slopes of these lines are larger than for the aluminium beads. This is expected, since the aluminium beads offer a much smaller thermal resistance, resulting in a smaller temperature drop across the porous layers. On the other hand, the temperature profiles in the fluid layers indicate strong thermal convection. In figure 2 (configuration 1), there are thermal boundary layers along the heated wall and the fluid/porous-layer interface, while the core region of the fluid layer is thermally stratified. This behaviour is less pronounced for configuration 2 (figure 3), where the vertical porous layer divides the enclosure into two fluid layers. Here, the temperature profiles in the core regions of the fluid layers show that some heat is conducted directly across the fluid layers, i.e. the core is not thermally stratified. This is expected because of the larger aspect ratio of each individual fluid layer when compared to the fluid layer of configuration 1. As shown in figure 4, the temperature profiles in the fluid layer of configuration 3 indicate, again, strong natural convection with a thermally stratified core region. The temperature profile at $\eta = 0.554$ is taken directly above the porous layer. It shows that there exists strong cross-flow along the fluid/porous-layer interface. The differences between the heat transfer patterns in the fluid layers of experiments 1 and 2 (figures 2a and b) as well as 3 and 4 (figures 3a and b) are mainly due to the different temperature drops across the porous layers (because of the large differences in the
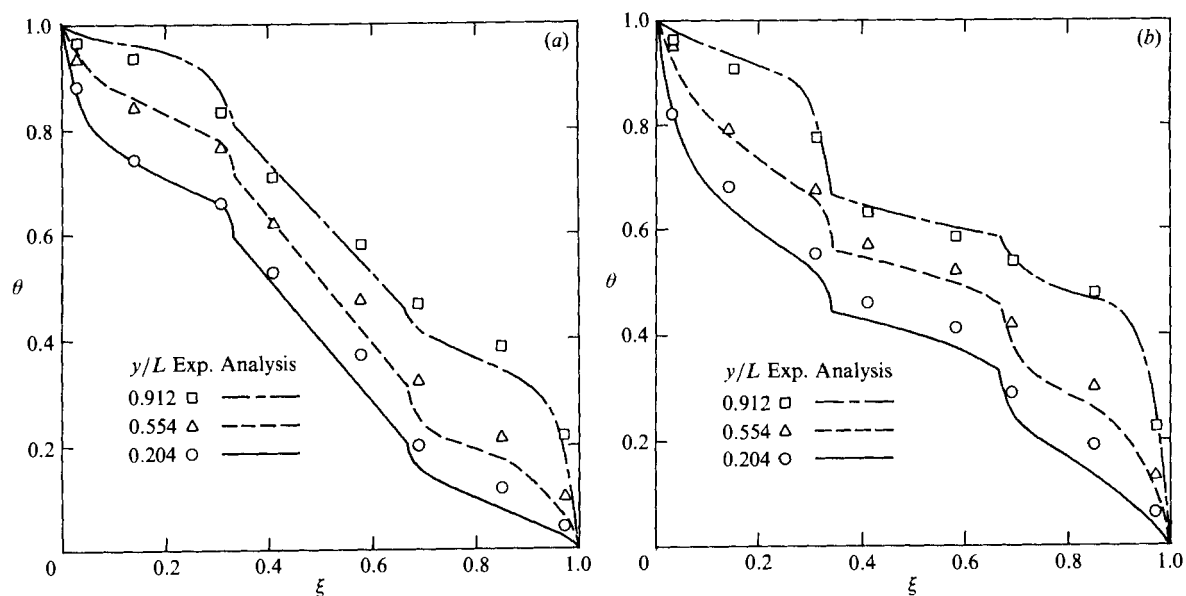
FIGURE 3. Experimental and predicted temperature profiles for configuration 2: (a) Experiment 3; (b) Experiment 4.
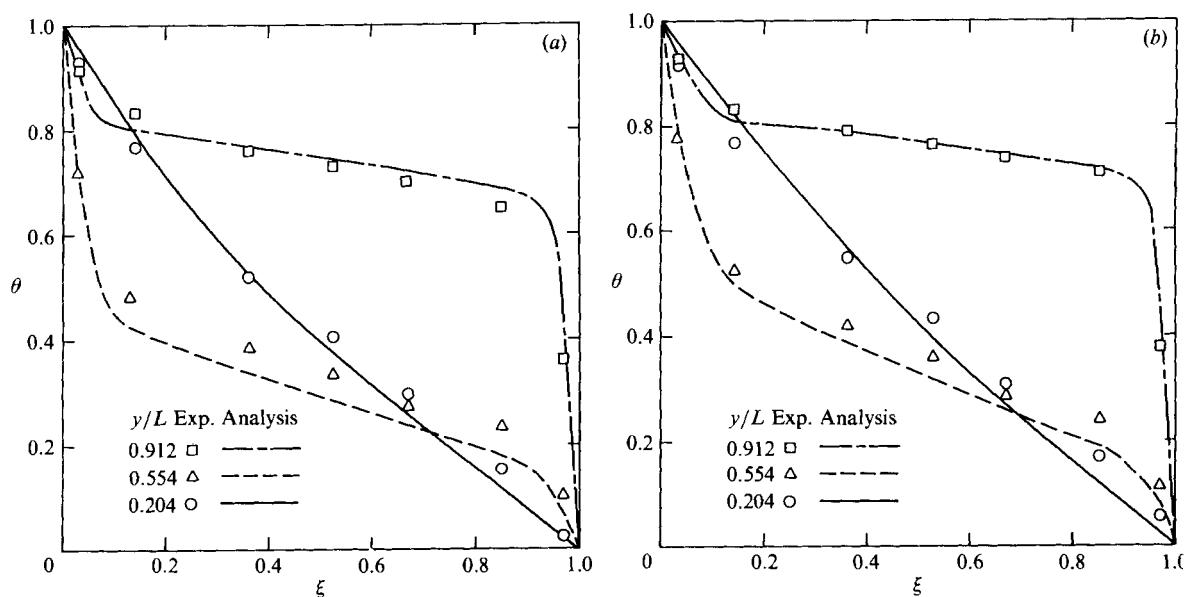

FIGURE 4. Experimental and predicted temperature profiles for configuration 3: (a) Experiment 5; (b) Experiment 6.

thermal conductivity ratios). In addition, the discontinuities in the slopes of the temperature profiles at the fluid/porous-layer interfaces are more pronounced in the case of the aluminium beads. On the other hand, in configuration 3 (figures 4a and b) the temperature profiles in both the fluid and porous layers are very similar for the glass and aluminium beads. In both cases, the porous and the fluid layers extend from the hot to the cold wall, resulting in the same total temperature drop across the

layers regardless of the porous material, the only difference being in the relative amounts of heat conducted through the porous layers.

The agreement between the measured and predicted temperatures is, in most cases, better than 5% of the total temperature difference across the test cell. The differences in the temperature distributions between the various configurations and porous materials are well predicted by the numerical model. Some of the discrepancies are possibly due to inaccuracies in determining the exact position of the movable thermocouple probe (± 0.5 mm), especially within the porous medium. In addition, non-uniformities in the porosity in the vicinity of the walls are expected to produce channelling of the flow along the walls which is not modelled in the present analysis. This can be seen, for example, in the measured temperature profiles at $\eta = 0.204$ in configuration 3 (figures 4a and b). The temperatures near the hot and cold walls deviate slightly from the predicted pure-conduction pattern indicating that adjacent to the walls bounding the porous layer some heat is transferred convectively. Some experimental error might also be due to the non-uniformities in the hot and cold wall temperatures (less than 3%) and imperfect adiabatic boundary conditions at the top and bottom walls. A possible error in the predicted results might be due to the uncertainty in the calculated effective thermal conductivity of the porous media (equation (11)). This problem is especially serious in the case of the aluminium beads, where small changes in the porosity produce large differences in the effective thermal conductivity. By comparing the slopes of the measured and predicted temperature profiles in the porous layers, it can be seen, however, that the calculated effective thermal conductivities are in reasonable agreement with the ones that can be inferred from the measurements. Finally, some inaccuracies in the predicted results may be associated with the temperature dependency of the thermophysical properties. In particular, the dynamic viscosity of glycerin varies by more than a factor of two over the temperature range of the present experiments (i.e. 10 °C). In view of the above uncertainties in the measurements and predictions, the agreement between the results can be considered very good.

4.2. Interferometric results

Interferometric measurements were performed using the smaller test cell with water as the fluid. For each configuration of the porous layer (refer to figure 1), four different porous media were utilized: 1.5 cm and 6.0 mm diameter glass beads as well as 3.16 mm and 6.35 mm diameter aluminium beads (see table 1, experiments 7–18). Since the temperature difference between the hot and cold walls was maintained at 2 °C, the Rayleigh (and Prandtl) number are the same for all experiments. On the other hand, owing to the different diameters of the beads, the Darcy number changes from 7.24×10^{-7} (for the small glass beads) to 1.53×10^{-5} (for the large aluminium beads). Again, the thermal-conductivity ratio differs greatly between the glass and the aluminium beads. Each experiment was supplemented by numerical simulations using the dimensionless parameters given in table 1. The interferometric results, together with the predicted isotherms and streamlines, are shown for each experiment in figures 5–16.

Since the index of refraction of water varies approximately linearly with temperature, the distances between the fringes (dark lines) on the interferograms (figures 5a–16a) correspond to about equal (and constant) temperature differences in the fluid. Also, note that the interferograms represent averages along the test beam over the depth of the test cell. Although no attempt was made to match the predicted isotherms (figures 5b–16b) with the isotherms that correspond to the interference
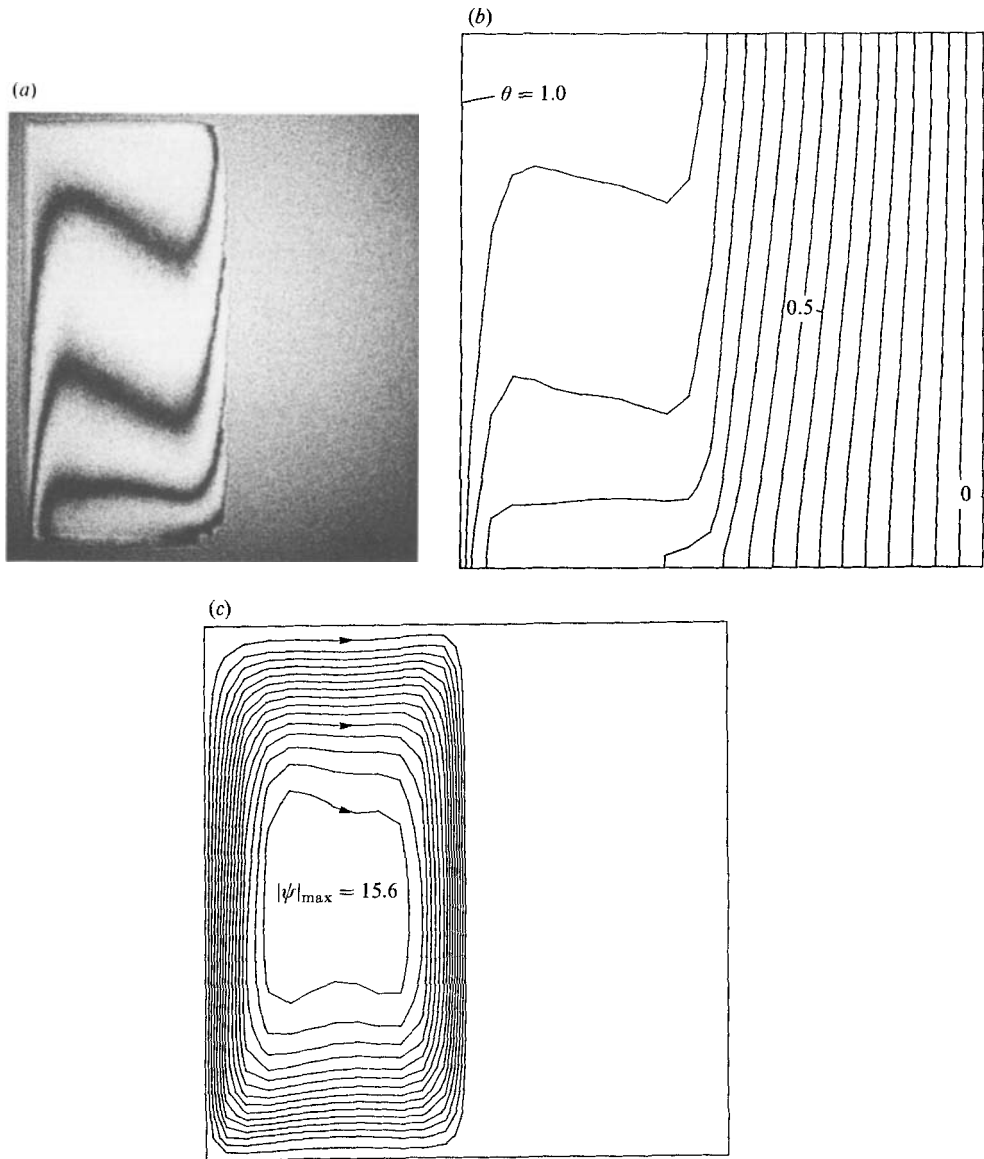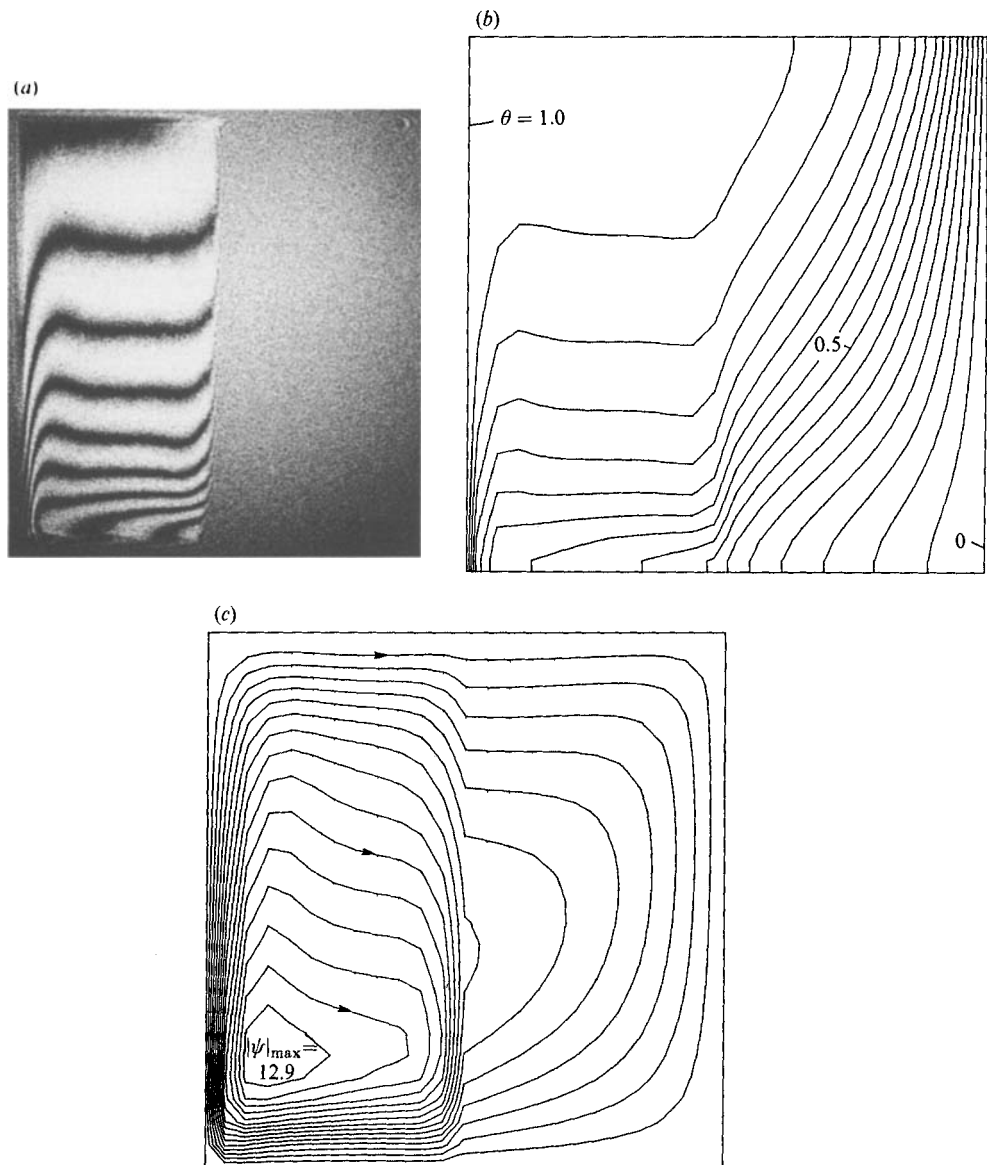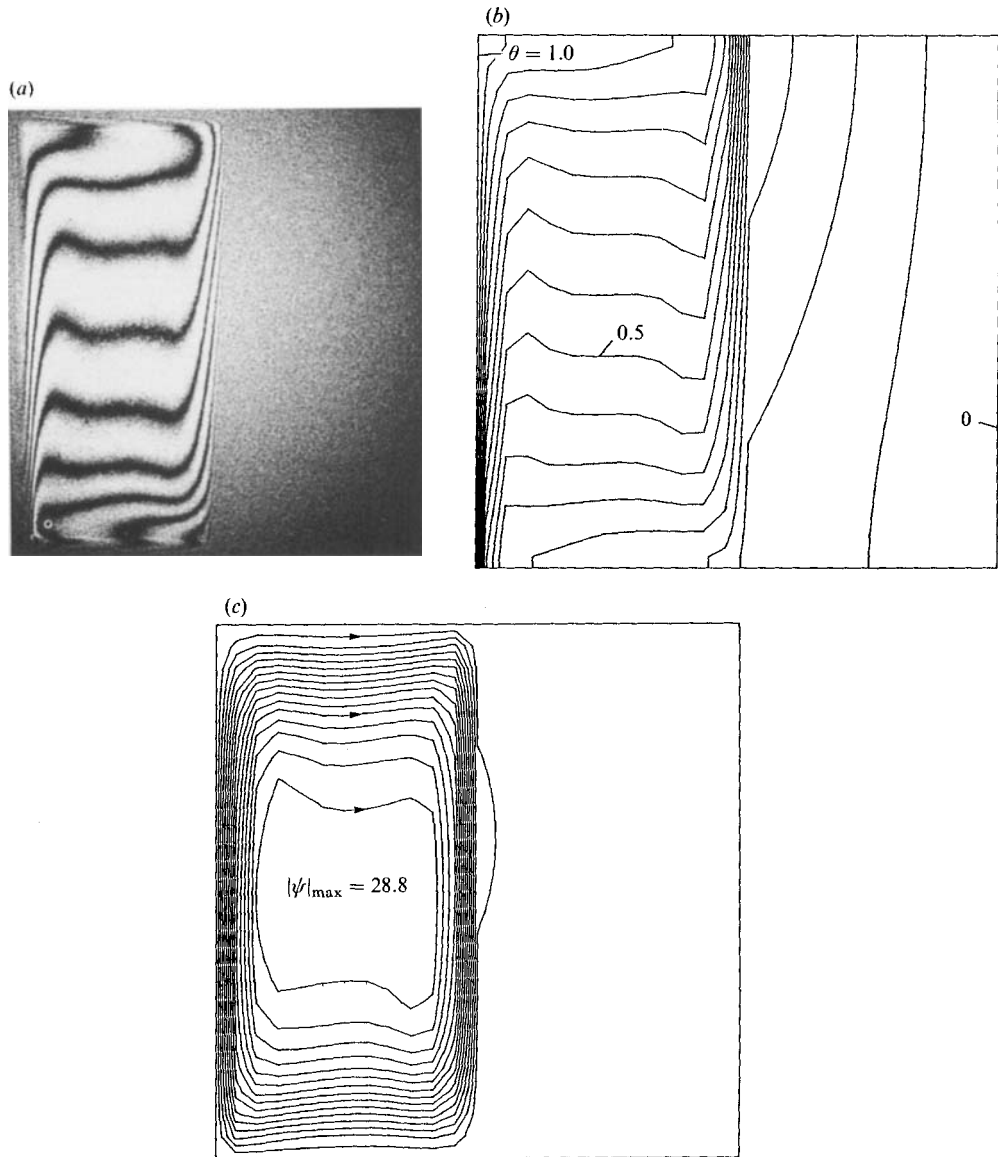
FIGURE 5. Experimental and predicted results for configuration 1, experiment 7: (a) photograph of interference fringe patterns; (b) predicted isotherms (equal increments); (c) predicted streamlines (equal increments).

fringes in the interferograms, a qualitative comparison of the measured and predicted isotherms shows that the present model predicts well the temperature distributions in the fluid layers for all the experiments. The predicted slopes and the spacings of the isotherms are in excellent agreement with the interferometric results. Any differences between the predicted and measured isotherms can, again, be attributed to the uncertainties in the experiments and the model as discussed in §4.1 (i.e. channelling of the flow, effective thermal conductivity, imperfect constant temperature and adiabatic boundary conditions, etc.). Since the predicted and interferometric results are in such good agreement, the following discussion of the

FIGURE 6. Experimental and predicted results for configuration 1, experiment 8: (*a*) photographs of interference fringe patterns; (*b*) predicted isotherms (equal increments); (*c*) predicted streamlines (equal increments).

physical phenomena occurring in the experiments applies to both the numerical and measured results and no reference is made to the specific method of obtaining them. In addition, owing to the strong coupling of the heat transfer and fluid flow in the present natural-convection system, it may be inferred that the predicted streamlines (figures 5*c*–16*c*) closely match the flow patterns in the experiments. This has also been confirmed through flow-visualization experiments reported in another study (Beckermann *et al.* 1986*a*).
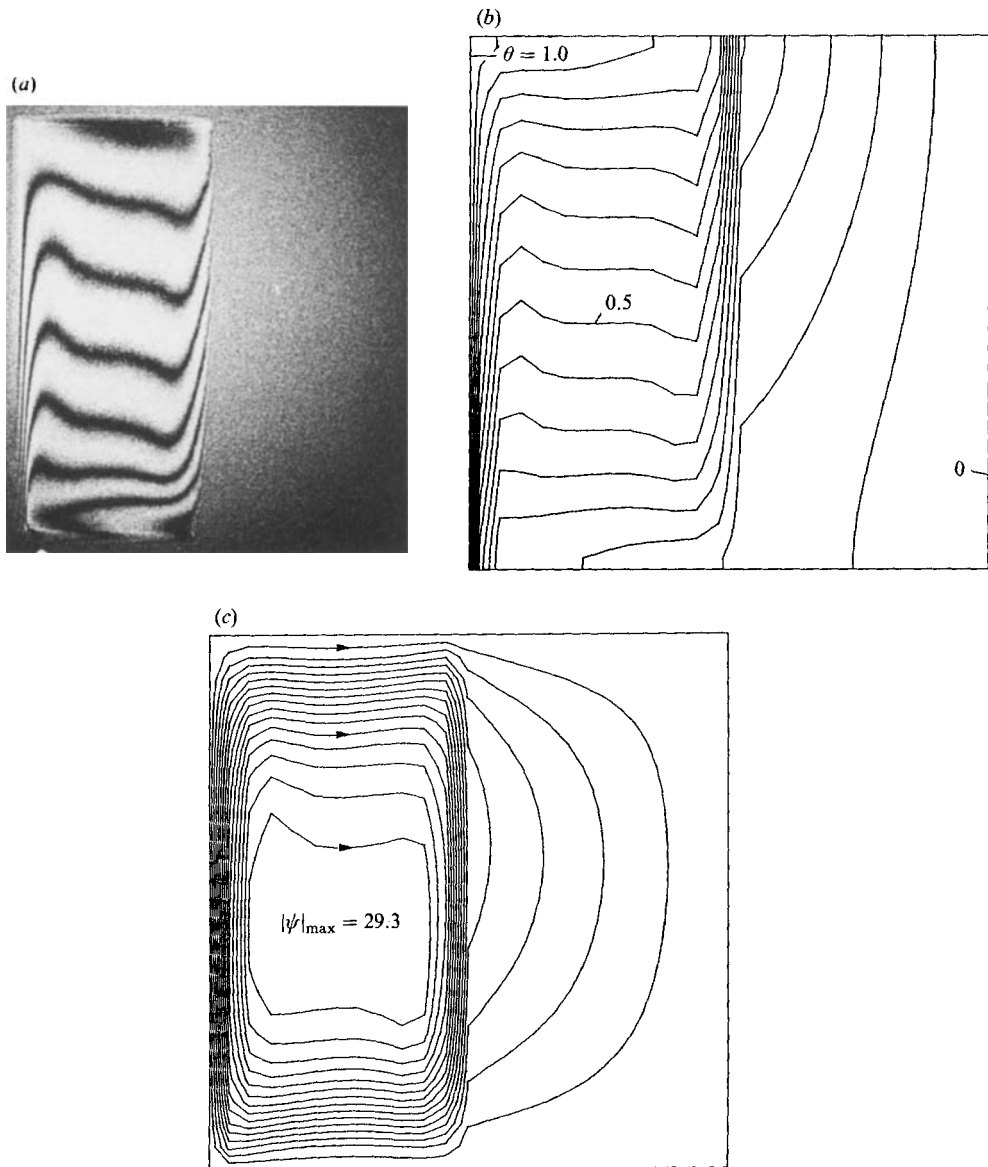
FIGURE 7. Experimental and predicted results for configuration 1, experiment 9: (*a*) photograph of interference fringe patterns; (*b*) predicted isotherms (equal increments); (*c*) predicted streamlines (equal increments).

Configuration 1

Shown in figures 5–8 are the results for configuration 1 where a vertical porous layer occupies one half of the test cell. In the cases of the small glass and aluminium beads (figures 5 and 7 respectively), the flow is almost completely confined to the fluid layer and is not able to penetrate into the porous layer. A boundary layer exists at the fluid/porous-layer interface. The heat transfer in the porous layer is mainly by conduction, as can be seen from the vertical and equally spaced isotherms. In the fluid layer, the flow and heat transfer is similar to natural convection in an enclosure of the same aspect ratio as the fluid layer. In the experiment with the small glass
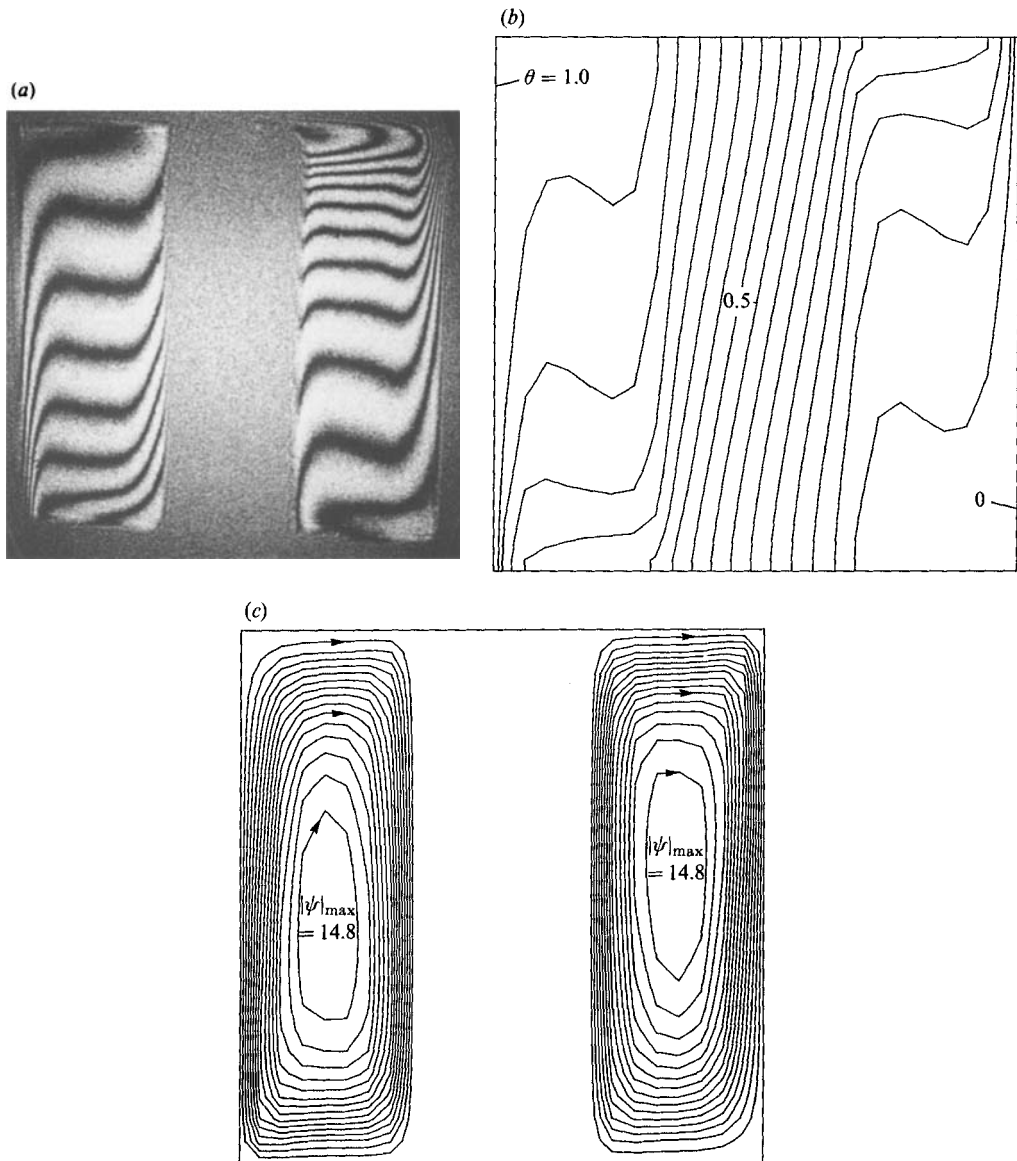
FIGURE 8. Experimental and predicted results for configuration 1, experiment 10: (a) photograph of interference fringe patterns; (b) predicted isotherms (equal increments); (c) predicted streamlines (equal increments).

beads, almost 90 % of the total temperature drop across the enclosure takes place in the porous layer, while for the small aluminium beads the porous layer offers very little thermal resistance to heat transfer and most of the temperature drop takes place in the fluid layer.

On the other hand, in the case of the large glass beads (figure 6), the porous layer offers much less resistance to the flow and natural convection takes place in the entire cavity. The streamlines show sharp changes in slope at the fluid/porous-layer interface. When the flow enters the porous layer at the upper region of the test cell, the streamlines bend upwards. Owing to the strong downflow along the fluid/porous-

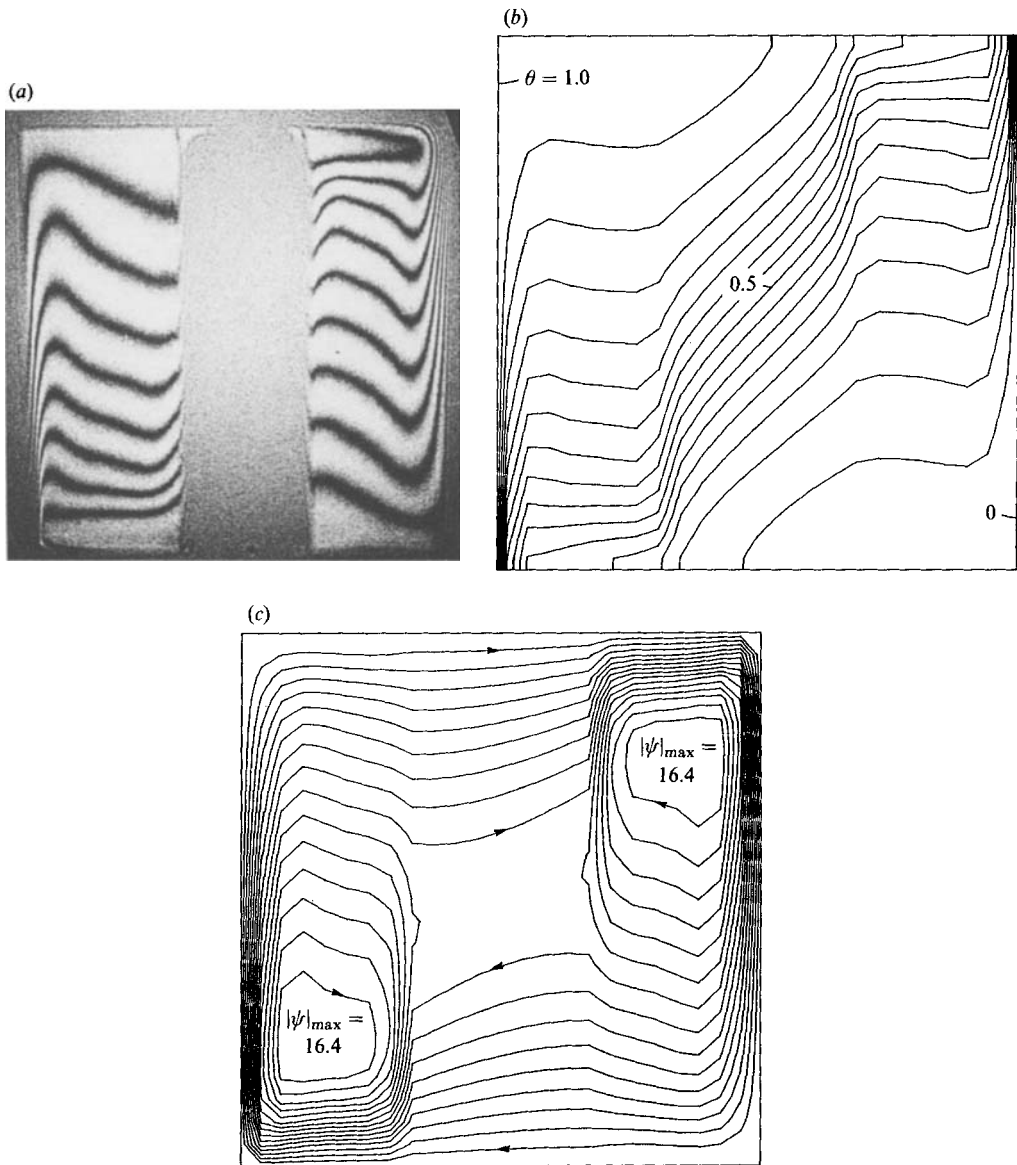FIGURE 9. Experimental and predicted results for configuration 2, experiment 11: (a) photograph of interference fringe patterns; (b) predicted isotherms (equal increments); (c) predicted streamlines (equal increments).

layer interface, the streamlines bend downwards when the flow leaves the porous region. The above observations indicate that the porous matrix exerts a strong influence on the velocity component parallel to the interface (resulting in a high velocity gradient on the fluid side), while the normal velocity component is relatively unaffected. Both velocity components are actually continuous across the fluid/ porous-layer interface. The centre about which the flow circulates is moved towards the lower left corner of the fluid layer (for natural convection in a vertical cavity filled with a homogeneous medium the eddy centre lies at the middle of the cavity).

FIGURE 10. Experimental and predicted results for configuration 2, experiment 12: (*a*) photograph of interference fringe patterns; (*b*) predicted isotherms (equal increments); (*c*) predicted streamlines (equal increments).

The isotherms in the porous layer are more horizontal, indicating that the penetrating fluid causes the heat to be transferred convectively.

The results shown in figure 8 are particularly interesting. Although the permeability (and Darcy number) of the porous layer in the case of the large aluminium beads is greater than for the large glass beads, much less fluid penetrates into the porous layer and, similar to the small aluminium beads, most of the flow and temperature drop takes place in the fluid layer. This can be explained by the fact that owing to the high effective thermal conductivity of the porous layer, the heat is
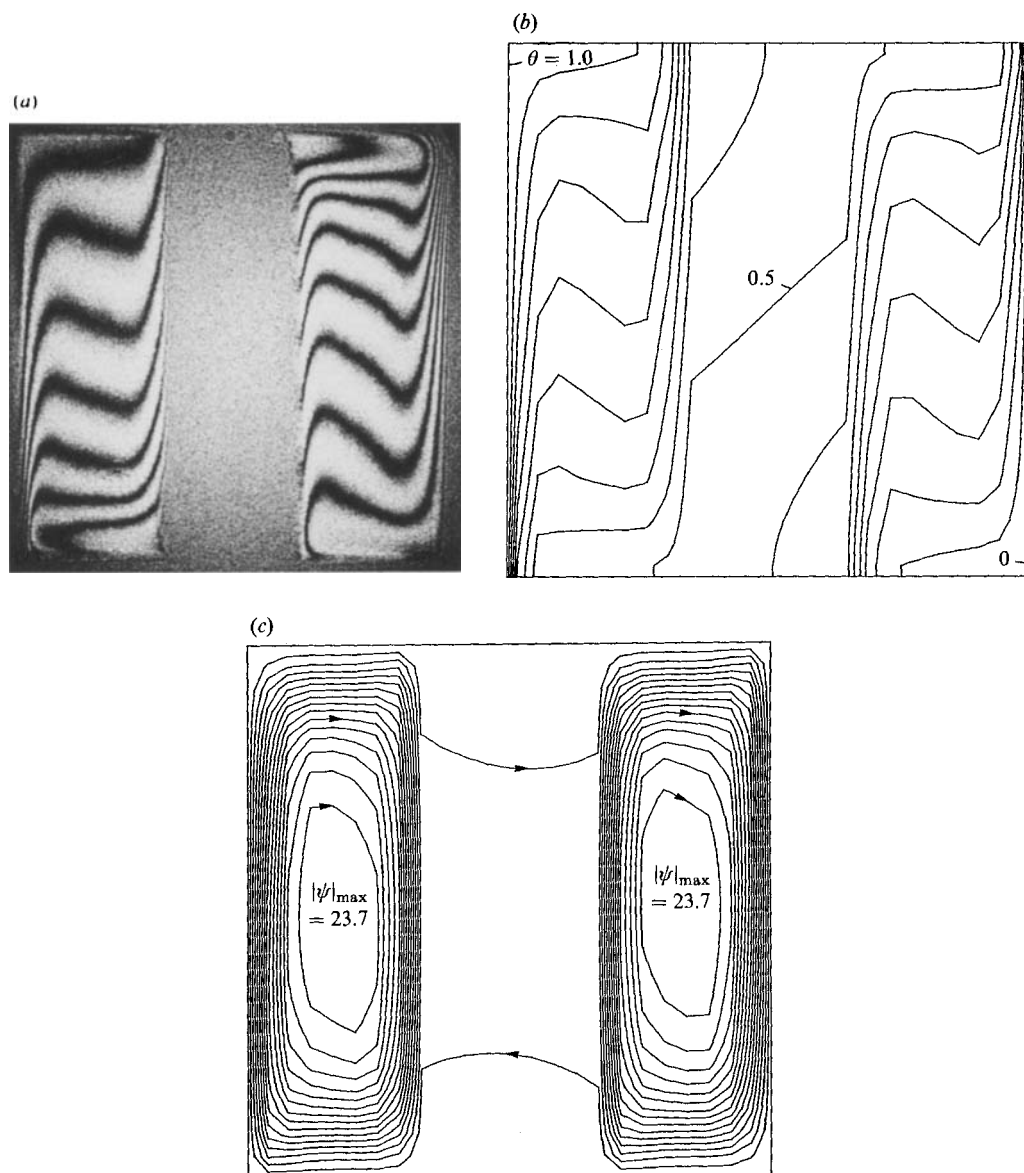
FIGURE 11. Experimental and predicted results for configuration 2, experiment 13: (a) photograph of interference fringe patterns; (b) predicted isotherms (equal increments); (c) predicted streamlines (equal increments).

transferred more effectively by conduction than by convection. In other words, temperature differences in the fluid within the porous layer are equalized by heat conduction through the solid matrix (i.e. the aluminium beads). Hence, the fluid becomes almost isothermal and natural convection is suppressed. It should also be noted that in the experiments with the aluminium beads, the fluid/porous-layer interface is not completely isothermal and the thermal-boundary-layer thickness (which can be inferred from the spacing of the isotherms) along the interface is larger than the one along the hot wall of the fluid layer. In addition, the isotherms show large discontinuities in slope at the fluid/porous-layer interface, which is due to the
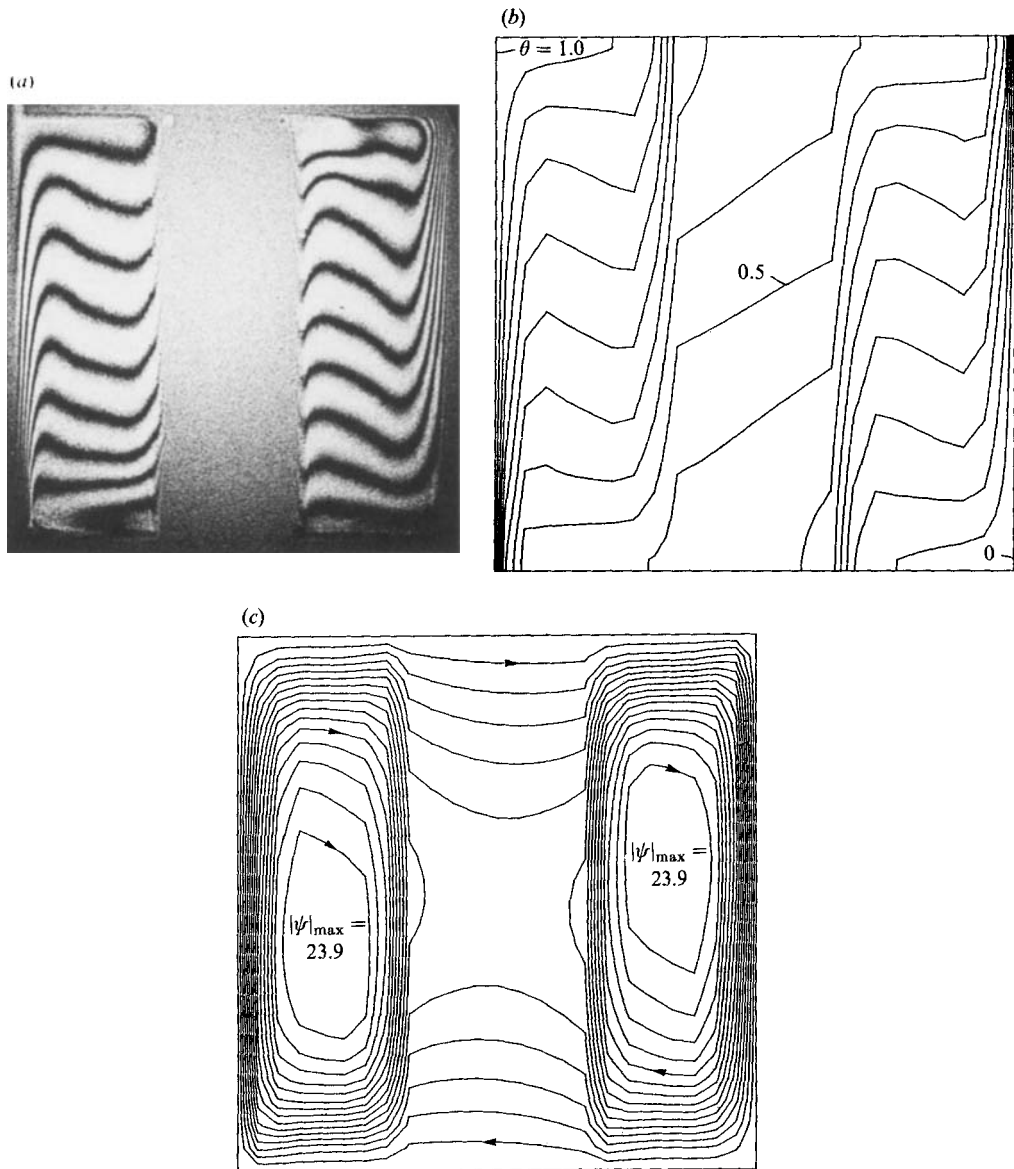
FIGURE 12. Experimental and predicted results for configuration 2, experiment 14: (*a*) photograph of interference fringe patterns; (*b*) predicted isotherms (equal increments); (*c*) predicted streamlines (equal increments).

high value of the effective thermal conductivity of the porous layer when compared to the thermal conductivity of the fluid.

Configuration 2

The results for configuration 2 are presented in figures 9–12. Here, the vertical porous layer occupies one-third of the test cell and is bounded by two vertical fluid layers of equal size. In general, the discussion about the heat transfer and fluid flow patterns in configuration 1 also applies to this configuration. Again, in the cases of the small glass and aluminium beads (figures 9 and 11 respectively) the flow cannot
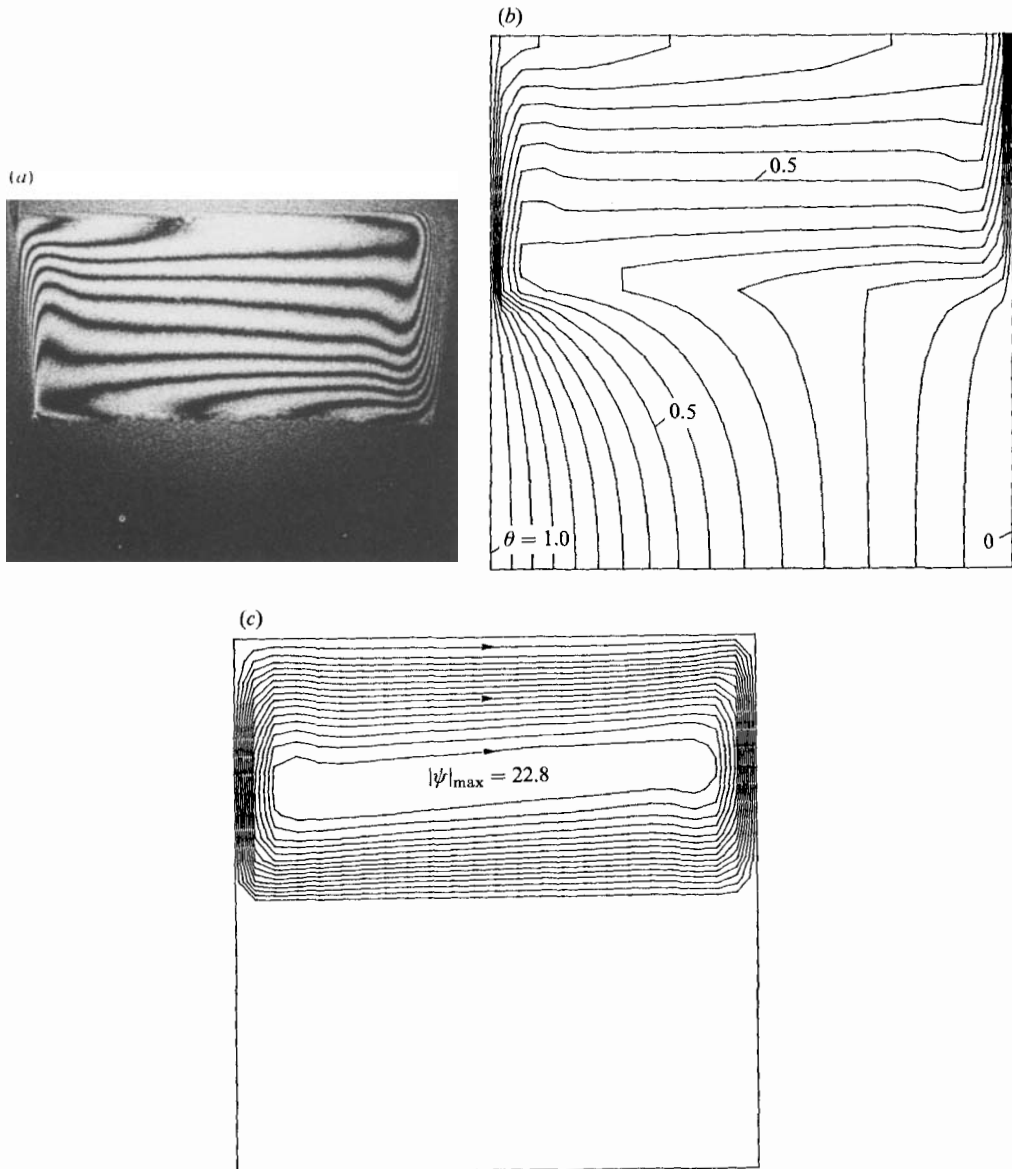
FIGURE 13. Experimental and predicted results for configuration 3, experiment 15: (a) photograph of interference fringe patterns; (b) predicted isotherms (equal increments); (c) predicted streamlines (equal increments).

penetrate through the porous layer and is confined to the fluid layers. In the case of the large glass beads (figure 10) natural convection takes place in the entire cavity, but with the large aluminium beads (figure 12) there is very little flow in the porous layer. In all experiments of configuration 2, there are two eddies in the test cell, the centre of each being in the fluid layers. In the case of the large glass beads, where a considerable amount of fluid flows through the porous layer, the eddy centres are moved towards the lower and upper regions of the left and right fluid layers respectively, while a stagnant region exists in the centre of the porous layer.

As in configuration 1, the porous layer in the experiment with the small glass beads
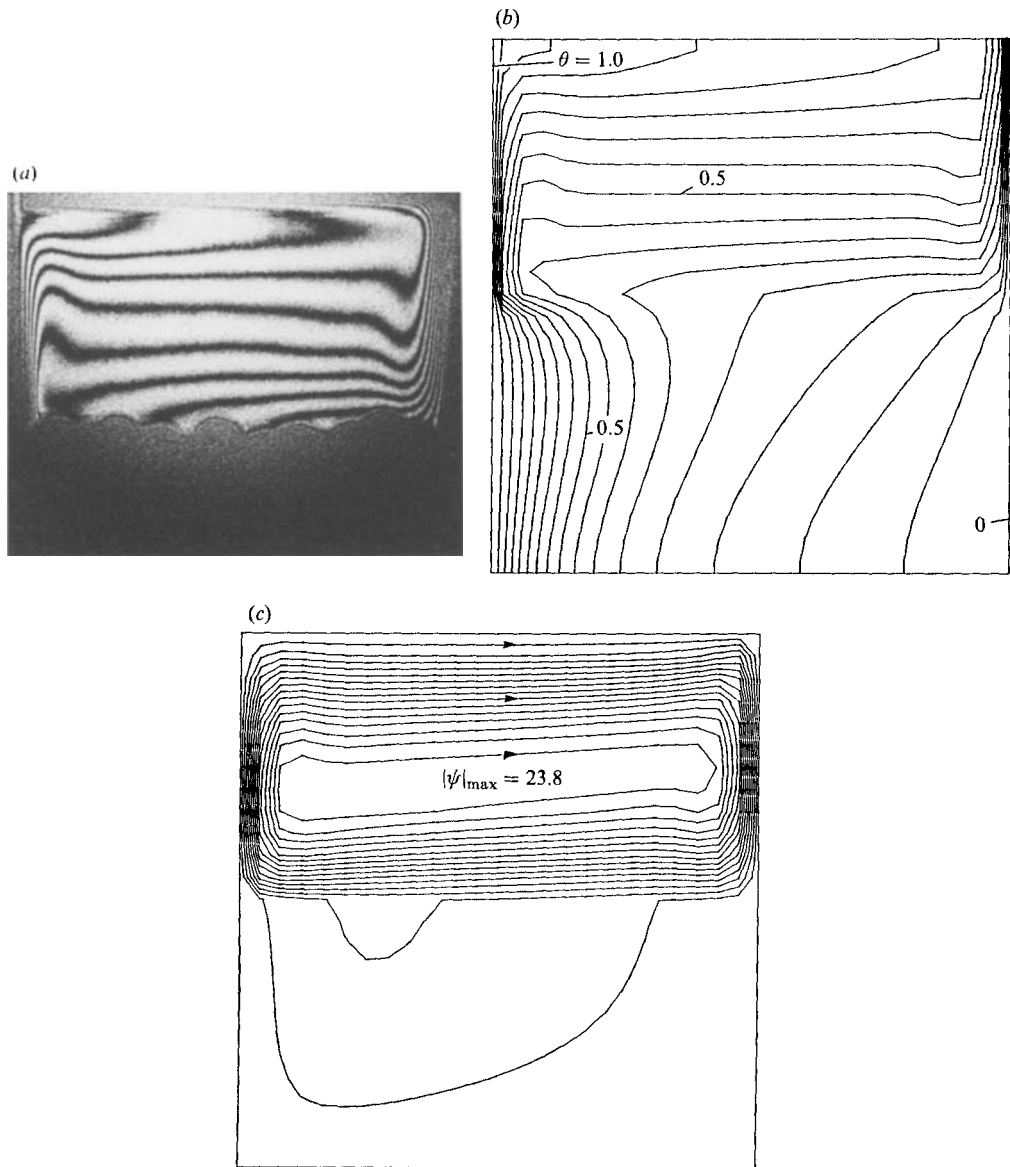
FIGURE 14. Experimental and predicted results for configuration 3, experiment 16: (*a*) photograph of interference fringe patterns; (*b*) predicted isotherms (equal increments); (*c*) predicted streamlines (equal increments).

offers a large thermal resistance to the heat transfer. Owing to the large temperature drop in this porous layer (relative to the total temperature drop across the test cell), natural convection in the fluid layers is weaker than in the experiments with the aluminium beads. In both experiments with the glass beads, the upper left and the lower right corners of the test cell are fairly isothermal, indicating that the fluid has reached the same temperature as the hot (left) and cold (right) walls. In the experiments with the aluminium beads, the isotherms in the porous layer are straight lines, except in the upper and lower parts where some convection takes place. These isotherms are almost horizontal, showing that heat is conducted from the top to the
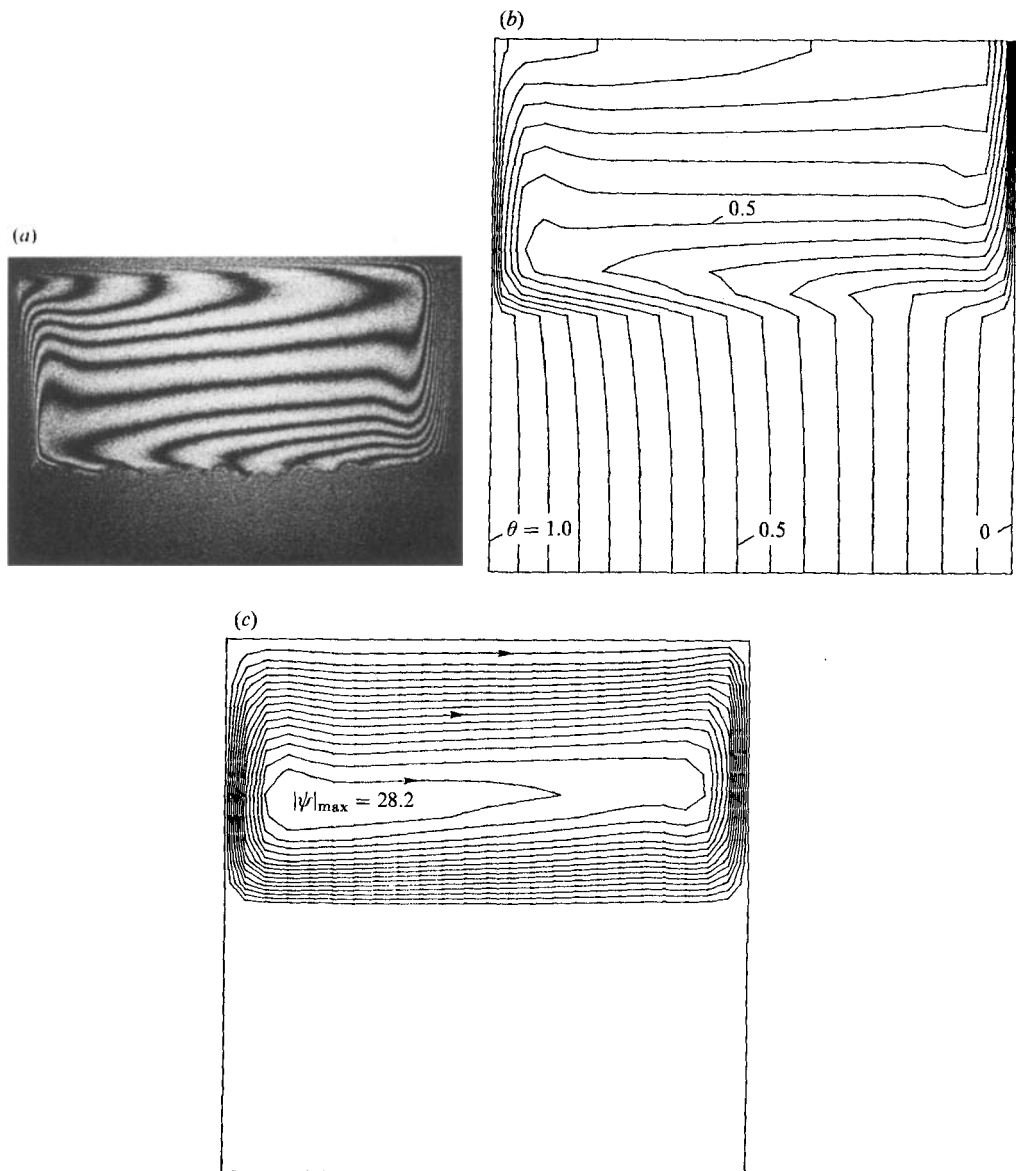
FIGURE 15. Experimental and predicted results for configuration 3, experiment 17: (a) photograph of interference fringe patterns; (b) predicted isotherms (equal increments); (c) predicted streamlines (equal increments).

bottom region of the porous layer, rather than directly from the left (hot) to the right (cold) side of the test cell. Obviously, this behaviour is induced by the natural-convection patterns in the neighbouring fluid layers, which tend to convect heat downwards and upwards along the left and right fluid/porous-layer interfaces respectively.

Configuration 3

For the case where a horizontal porous layer occupies the lower half of the test cell (configuration 3), the results are presented in figures 13–16. From the streamlines,
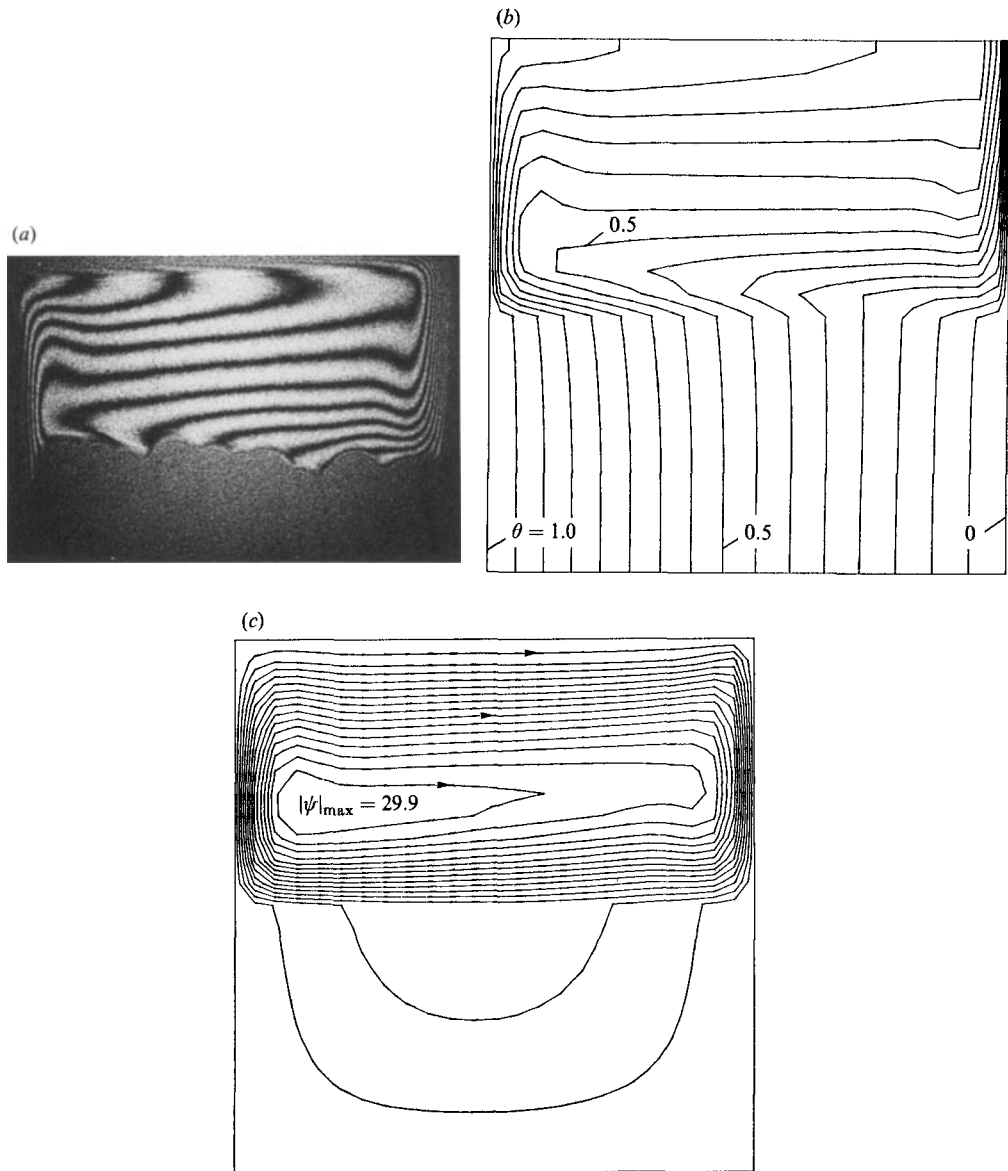
FIGURE 16. Experimental and predicted results for configuration 3, experiment 18: (a) photograph of interference fringe patterns; (b) predicted isotherms (equal increments); (c) predicted streamlines (equal increments).

shown in figures 13 (c)–16 (c), it can be seen that in all experiments there is very little penetration of fluid into the porous layer, when compared to configurations 1 and 2. In other words, the streamline patterns are very similar to the ones that would be expected in an enclosure of the same aspect ratio as the fluid layer. In the experiments with the aluminium beads (figures 15 and 16), the centres of the circulation patterns are slightly moved towards the hot (left) wall of the enclosure, which can be attributed to strong heat conduction in the porous layer acting as the lower 'wall' of the fluid layer. The comparatively small extent of penetration of fluid into the porous layers in configuration 3 can be explained by the fact that the fluid

can convect heat from the hot to the cold wall without having to flow through a porous medium. In addition, the path of fluid flowing through the porous medium from the cold to the hot wall is longer than the paths in the cases of the vertical porous layers. Hence, fluid penetrating into the porous layer would experience a larger resistance and tends to 'avoid' the porous layer completely.

The isotherms in the porous layers of the experiments with the aluminium beads (figures 15b and 16b) are vertical and equally spaced, indicating that heat is transferred by conduction directly from the hot to the cold wall. Even though strong natural convection exists in the adjoining fluid layer, the isotherms close to the fluid/porous-layer interface are not distorted. On the other hand, the isotherms in the porous layers of the experiments with the glass beads (figures 13b and 14b) are highly curved and the isotherms in the fluid layer merge more gradually into the isotherms of the porous layer. Since this distortion also exists in the case of the small glass beads, it can be concluded that the curvature of the isotherms in the porous layer is not primarily due to penetration of fluid into the porous layer, but is also caused by natural convection on the fluid side of the fluid/porous-layer interface.This coupling of the isotherm patterns in the two layers is more pronounced in the experiments with the glass beads, because the thermal-conductivity ratio R_k is close to unity, causing the temperature gradients on both sides of the fluid/porous-layer interface to be more similar when compared to the experiments with the aluminium beads. Also, note that a thermal boundary layer exists on the fluid side of the fluid/porous-layer interface in all experiments of configuration 3, except in the case of the large glass beads, where the (small amount of) fluid penetrating into the porous layer prevents the thermal boundary layer from being formed.

5. Conclusions

A fundamental study has been performed of natural convection in a vertical enclosure containing simultaneously fluid and porous layers. In the analytical part of the study, a model is developed which treats the fluid and porous regions as a single domain. Mathematically, this is achieved by assuming continuity of the velocities, stresses, temperatures and heat fluxes at the fluid/porous-medium interface and combining the governing equations for the fluid and porous regions into a single set of conservation equations valid for the entire domain. This method results in considerable simplifications in the numerical solution procedure, since the matching conditions at the fluid/porous-medium interface are satisfied automatically. The model is successfully validated through temperature measurements and interferometric results obtained for three configurations of the porous layer and wide ranges of the governing dimensionless parameters. A discussion of the experimental uncertainties and the deficiencies in the present model (as evident from the comparison of the experimental and predicted results) is presented in §4.1. From an examination of the physical phenomena occurring in the experiments, the following major conclusions can be drawn.

(i) The intensity of natural convection is always much stronger in the fluid regions than in the porous medium. The degree of penetration of fluid into the porous layer increases with increasing permeability (i.e. Darcy number) as well as with increasing Rayleigh number.

(ii) If penetration takes place, the fluid flow patterns in the fluid layer are significantly altered when compared to natural convection in an enclosure of the

same aspect ratio as the fluid layer. The streamlines show sharp cusps at the fluid/porous-medium interfaces.

(iii) A high effective thermal conductivity suppresses natural-convection flow in the porous medium because heat is transferred more effectively by conduction. In this case, the temperature drop across the (vertical) porous layer is relatively small, while the fluid layer represents the major thermal resistance to heat transfer.

(iv) For a high thermal-conductivity ratio R_k the isotherms show large discontinuities in slope at the fluid/porous-medium interface. On the other hand, a thermal-conductivity ratio close to unity causes strong coupling between the isotherm patterns in the fluid and the porous layers.

(v) In the case of a horizontal porous layer extending over the entire length of the enclosure, the extent of penetration of fluid into this porous layer is small when compared to a vertical porous layer of the same size and for the same values of the governing parameters, because the fluid can convect heat from the hot to the cold wall without having to flow through a porous medium.

REFERENCES

ARQUIS, E. & CALTAGIRONE, J. P. 1984 *C. R. Acad. Sci. Paris* **299**, 1.

ARQUIS, E., CALTAGIRONE, J. P. & LANGLAIS, C. 1986 In *Heat Transfer 1986*, pp. 2653–2658. Hemisphere.

BEAVERS, G. S. & JOSEPH, D. D. 1967 *J. Fluid Mech.* **30**, 197.

BECKERMANN, C., RAMADHYANI, S. & VISKANTA, R. 1986a In *Natural Convection in Porous Media* (ed. V. Prasad & N. A. Hussain), pp. 1–13. ASME.

BECKERMANN, C., VISKANTA, R. & RAMADHYANI, S. 1986b *Numer. Heat Transfer* **10**, 557.

BRINKMAN, H. C. 1949 *Appl. Sci. Res. Suppl.* **2–4**, 190.

CATTON, I. 1985 In *Natural Convection: Fundamentals and Applications* (ed. W. Aung, S. Kakac & R. Viskanta), pp. 514–547. Hemisphere.

COMBARNOUS, M. A. & BORIES, S. A. 1975 In *Advances in Hydroscience 10* (ed. V. T. Chow), pp. 231–307. Academic.

DERJANI, G., TASLIM, M. E. & NARUSAWA, U. 1986 In *Natural Convection in Enclosures-1986* (ed. R. S. Figliola & I. Catton), pp. 83–89. ASME.

ERGUN, S. 1952 *Chem. Engng Prog.* **48**, 98.

FORCHHEIMER, P. 1901 *Z. Ver. Deutsch. Ing.* **45**, 1782.

GJERDE, K. M. & TYVAND, P. A. 1984 *Intl J. Heat Mass Transfer* **27**, 2289.

KIM, S. & RUSSEL, W. B. 1985 *J. Fluid Mech.* **154**, 269.

KOPLIK, J., LEVINE, H. & ZEE, A. 1983 *Phys. Fluids* **26**, 2864.

LUNDGREN, T. S. 1972 *J. Fluid Mech.* **51**, 273.

MASUOKA, T. 1974 *Bull. Japan Soc. Mech. Engrs* **17**, 232.

McKIBBIN, R. & O'SULLIVAN, M. J. 1981 *J. Fluid Mech.* **111**, 141.

NEALE, G. & NADER, W. 1974 *Can. J. Chem. Engng* **52**, 475.

NIELD, D. A. 1977 *J. Fluid Mech.* **81**, 513.

NIELD, D. A. 1983 *J. Fluid Mech.* **128**, 37.

NISHIMURA, T., TAKUMI, T., SHIRAISHI, M., KAWAMURA, Y. & OZOE, H. 1986 *Intl J. Heat Mass Transfer*, **29**, 889.

PATANKAR, S. 1980 *Numerical Heat Transfer and Fluid Flow*. Hemisphere.

POULIKAKOS, D. & BEJAN, A. 1983 *Intl J. Heat Mass Transfer* **26**, 1805.

RANA, R., HORNE, R. N. & CHENG, P. 1979 *Trans. ASME C: J. Heat Transfer* **101**, 411.

REDA, D. C. 1985 In *Heat Transfer in Porous Media and Particulate Flows* (ed. L. S. Yao *et al.*), pp. 31–39. ASME.

SOMERTON, C. W. & CATTON, I. 1982 *Trans. ASME C: J. Heat Transfer* **104**, 160.

SOMERTON, C. W. & GOFF, J. D. 1985 In *Heat Transfer in Porous Media and Particulate Flows* (ed. L. S. Yao *et al.*), pp. 111–119. ASME.

WEAVER, J. A. 1985 Solid–liquid phase change heat transfer in porous media. MSME thesis, Purdue University, West Lafayette, IN.